Effects of nanostructuring and substrate symmetry on antiferromagnetic domain structure in LaFeO_{3} thin films

E. Folven, A. Scholl, A. Young, S. T. Retterer, J. E. Boschker, T. Tybell, Y. Takamura, and J. K. Grepstad

Phys. Rev. B **84**, 220410 — Published 28 December 2011

DOI: 10.1103/PhysRevB.84.220410

Effects of nanostructuring and substrate symmetry on antiferromagnetic domain structure in $LaFeO_3$ thin films

Authors: E. Folven,[1,*] A. Scholl,[2] A. Young,[2] S.T. Retterer,[3] J. E. Boschker,[1] T. Tybell,[1] Y. Takamura,[4] and J.K. Grepstad[1]

[1] Department of Electronics and Telecommunications, Norwegian University of Science and Technology, NO-7491 Trondheim, Norway

[2] Advanced Light Source, Lawrence Berkeley National Laboratory, Berkeley, CA 94720, USA

[3] Oak Ridge National Laboratories, P.O. Box 2008 MS 6123, Oak Ridge, TN 37831, USA

[4] Department of Chemical Engineering and Materials Science, University of California-Davis, Davis, CA 95616, USA

Abstract

The antiferromagnetic domain structure in $LaFeO_3$ thin film epilayers grown on $La_{0.7}Sr_{0.3}MnO_3$ is imaged combining linearly polarized X-ray absorption spectroscopy with photoemission electron microscopy. Detailed analysis of polarization-dependent domain contrast from magnetic dichroism reveals two sets of symmetrically different antiferromagnetic *easy axes* in the $LaFeO_3$ layer along the in-plane <110> and <100> crystalline axes (pseudocubic notation), respectively. We show that extended antiferromagnetic domains can be stabilized selectively for nanowires defined in this perovskite thin film system along either orientation of the *easy axes*. The results demonstrate how the equilibrium domain structure of thin film nanoscale antiferromagnets depend on a combination of substrate symmetry, nanowire dimensions, and in-plane crystalline orientation.

The possibility to control magnetism in thin films and multilayers of perovskite oxides by epitaxial strain,[1-3] oxygen stoichiometry,[4-7] chemical substitution,[8, 9] and substrate crystalline symmetry[10, 11] has rendered such materials important model systems for fundamental studies of magnetic structure as well as attractive candidates for device applications. Advances in fabrication of complex oxide thin film nanostructures[12] and the recent development of novel tools for magnetic imaging with high spatial resolution have made the study of such systems on the nanometer length scale a realistic endeavor.[13] Stabilization of preferred directions of magnetization in ferromagnetic perovskite oxide nanostructures has been demonstrated, relying on strain[14] as well as shape.[15] However, the case for domain stabilization in antiferromagnetic materials is scarcely explored. Theoretical studies predict that magnetoelastic effects can drive shape-induced domain formation in finite-sized antiferromagnets.[16] We have recently reported experimental evidence for stabilization of extended antiferromagnetic (AFM) domains along edges of embedded $LaFeO_3$ (LFO) thin film nanostructures, i.e., for edges aligned with *easy axes* of the LFO layer, only.[17] The functional properties of perovskite oxides (ABO_3) are intimately related to the structure of the BO_6 octahedral network.[18, 19] Recent reports discuss manipulation of the octahedral structure in perovskite thin film systems, and thus of their functional properties, using epitaxial strain.[11, 20] In this work, we show how the AFM easy axes are modified in epitaxial LaFeO3/La0.7Sr0.3MnO3 (LFO/LSMO) thin film bilayers, compared to LFO grown directly on (001)-oriented Nb-doped SrTiO3 (Nb:STO). Moreover, we demonstrate how the width and crystalline orientation of nanowires defined in these LFO/LSMO bilayers serve to stabilize extended AFM domains selectively along different easy axes.

The LFO/LSMO epitaxial bilayers were grown by pulsed laser deposition on (001)-oriented Nb:STO substrates (0.05 wt% Nb) to a total thickness of 100 unit cells (u.c.), with individual layer thicknesses of 10 u.c. LFO/90 u.c. LSMO, 20 u.c. LFO/80 u.c. LSMO, and 50 u.c. LFO/50 u.c. LSMO. The LSMO layer was grown at a substrate temperature of T_{sub} = 680 °C in an oxygen ambient of 2.0 x 10^{-1} mbar,

followed by the deposition of the LFO layer at T_{sub} = 520 °C in an oxygen ambient of 1.0 x 10^{-2} mbar. The KrF excimer laser was operated at 1 Hz with a fluence of ~2.0 J/cm^2 for deposition of LSMO and at 5Hz with a fluence of ~3.0 J/cm^2 for deposition of LFO. The growth was monitored with *in situ* reflection high-energy electron diffraction. Unit cell intensity oscillations of the specular reflection were observed throughout the growth. The out-of-plane lattice constants of the LFO and LSMO layers were determined from x-ray diffraction measurements at $(d_{001})_{pc}$ = 4.04 Å for LFO and $(d_{001})_{pc}$ = 3.85 Å for LSMO (pseudocubic notation). Distinct thickness fringes around the LFO$(001)_{pc}$ and LSMO$(001)_{pc}$ peaks and rocking curves widths comparable to that of the substrate (FWHM<0.02°) indicate excellent crystalline quality. Atomic force microscopy showed sub-monolayer surface roughness on the individual terraces of the step-and-terrace LFO film surface. Nanostructures were defined in these all-oxide magnetic bilayers using a patterning technique, relying on local disruption of the structural and magnetic order by Ar^+ ion implantation through a Cr hard-mask (for details, see refs. 17, 21). Imaging of the AFM domain structure was accomplished by combination of linearly polarized x-ray absorption spectroscopy with photoemission electron microscopy (PEEM) in the PEEM-3 microscope on beamline 11.0.1.1 at the Advanced Light Source, relying on x-ray magnetic linear dichroism (XMLD) at the Fe L_2 absorption edge for domain contrast.[22] The XMLD-PEEM images were recorded at photon energies of 722.7 eV and 720.9 eV, for which the magnetic dichroism in the Fe L_2 absorption multiplet has opposite sign. All images were obtained using linearly polarized x-rays incident on the sample at an angle of 30° with the sample surface. The x-ray polarization vector could be varied continuously from *s*- to *p*-polarization, i.e., from parallel to 60° inclination with the sample surface. The Curie temperature of the LSMO layer was determined from SQUID measurements at T_c ~ 270 K. The XMLD-PEEM data reported here for LFO were all taken at room temperature and thus without impact from magnetic interaction with the underlying LSMO layer.

The orientation of the Fe^{3+} spin axis in the AFM domains for a blanket film of the LFO/LSMO bilayer was established from XMLD-PEEM images recorded at different polarizations. The x-ray polarization vector was rotated in increments of 10°, from p-polarization (i.e., parallel to the plane of incidence) to s-polarization (i.e., perpendicular to the plane of incidence), with the angle ω of the ***E***-vector defined as 0° and 90° for p- and s-polarization, respectively. Figure 1(a) shows XMLD-PEEM images recorded for ω = 0°, 40°, and 90°, from a 5 μm x 5 μm region of the LFO[20u.c.]/LSMO[80u.c.] bilayer. The measurement geometry is indicated in the inset of Fig. 1(b), and the three domain images in Fig. 1(a) are all shown with the same contrast settings. A region which appears predominantly bright for ω = 90° is delineated (Fig. 1(a)) as a guide to the eye. This region displays uniform contrast for ω = 90° and ω = 0°. However, the contrast is weaker due to the 30° angle of incidence, and has the opposite sign, i.e., dark regions for ω = 90° are bright for ω = 0° and vice versa. For ω = 40°, on the other hand, the region splits up into smaller domains with noticeable difference in contrast. This observation suggests that the LFO layer comprises more than the two <100> oriented AFM domains typically reported for LFO grown on cubic STO.

Figure 1(b) shows a quantitative analysis of the XMLD intensity as a function of E-vector angle, ω. XMLD-PEEM images of an 8 μm x 8 μm region of the 20 u.c. LFO film were obtained for different orientations of the polarization vector, all with the x-rays incident along the $[110]_{pc}$ direction. In these images, the polarization dependence of the XMLD contrast was analyzed pixel-by-pixel. The resulting single pixel "polarization spectra" were noise filtered using *principal component analysis*.[23] From these noise filtered spectra, pixels showing a qualitatively similar polarization dependence were identified and the unfiltered values for these pixels were averaged. This data was then fitted to the expected $\cos^2\theta$ dependence of the XMLD signal for each type of domain,[22, 24, 25] where θ denotes the angle between the ***E***-vector and the AFM spin axis. The data in Fig. 1(b) supports the presence of four differently oriented domains. For one pair of XMLD intensity curves, the maximum difference in

contrast occurs for ω = 90°, little contrast around ω = 30°, and again distinct domain contrast, but with opposite sign for ω = 0°. These domains have their AFM spin axis aligned along $[110]_{pc}$ and $[-110]_{pc}$ directions. The second type of domains exhibit maximum difference in contrast for an ω between 40° and 50° and with nearly identical XMLD intensities for ω = 0° and 80°, which implies the AFM spin axis aligned along the $[100]_{pc}$ and $[010]_{pc}$ directions. Thus, with the measurement geometry in Fig. 1(b), maximum contrast for AFM domains with their spins oriented along the in-plane $<100>_{pc}$ and $<110>_{pc}$ axes is obtained for $\omega \sim 40°$ and $\omega \sim 90°$, respectively, Similar measurements taken with the x-rays incident along the <100> axis (not shown) preclude the possibility that the strong contrast observed at ω = 40° originates from domains with their AFM axis canting out of the LFO film plane. The quantitative analysis discussed here was carried out for LFO/LSMO bilayers with different LFO layer thicknesses (10 u.c., 20 u.c. and 50 u.c.). The same set of spin axis orientations was observed in all three samples. However, we find that the distribution of AFM domains between the two categories of degenerate AFM spin axes depends in the LFO thickness, cf. Fig. 1(c). The thinnest (10 u.c.) LFO layer showed a predominance of domains with the AFM spin axis along in-plane <110> directions. In the 20 u.c. LFO layer, the two types of domain orientation were almost equally populated, whereas the 50 u.c. LFO layer showed a slightly higher share of domains with the AFM axis along <100> directions. The inset in Fig. 1(c) shows the intensity of the XMLD signal as a function of LFO layer thickness for the two different categories of AFM domains (i.e., with their spin axis along $<110>_{pc}$ and $<100>_{pc}$, respectively). We note the increase in XMLD intensity with LFO layer thickness and the stronger dichroism of the $<100>_{pc}$-oriented domains.

The outcome of the above analysis differs from the reported alignment of AFM moments for 10 u.c. to 100 u.c. thick LFO films grown directly on (001)-oriented STO substrates. Previous work report the AFM spin axis to be aligned with the in-plane $<100>_{pc}$ crystalline axes of the substrate with an out-of-plane canting angle between 0 and 45°,[17, 22, 26, 27] the variation in canting angle being attributed to

different thin film growth techniques. The present results were obtained for LFO films grown on a different "effective" substrate (i.e., an LSMO layer deposited on single-crystalline Nb:STO). X-ray diffraction measurements for two LFO[100u.c.]/Nb:STO and LFO[100u.c.]/LSMO[50u.c.]/Nb:STO samples, grown under conditions identical to those of the bilayers discussed above, show films of high crystalline quality and near fully strained to the Nb:STO substrate. However, we do observe a slight shift in the q_x values of the LFO $(-204)_{pc}$ and $(204)_{pc}$ Bragg reflections relative to those of the Nb:STO $(-204)_c$ and $(204)_c$ reflections, when LFO is grown on top of LSMO, Fig. 2(a) and (b). This shift is not observed for LFO grown directly on Nb:STO, Fig. 2(c) and (d). The x-ray diffraction measurements indicate that the LFO assumes a tetragonal structure when grown directly on Nb:STO, but adopts a lower symmetry when grown on top of an LSMO buffer layer. In LFO, the superexchange interaction responsible for the AFM order[28, 29] is correlated with the rotations of the oxygen octahedra.[30] Furthermore, it has been shown that the orientation of the AFM spin axis in thin films is highly sensitive to minor changes in crystalline structure.[27, 31] Therefore, we contend that the observation of multiple AFM spin axis orientations in LFO thin films grown on LSMO/Nb:STO derives from changes in film symmetry.

Significant changes in the AFM domain configuration are observed when the present LFO epilayers are patterned into nanostructures, depicted schematically in Fig. 3(a). Figures 3(b)-(d) show XMLD-PEEM images for such zigzag-shaped nanowires of different widths, defined with their edges parallel to the in-plane $<110>_{pc}$ axes. The inset depicts the direction of the incident x-rays with respect to the in-plane orientation of the sample, and the images were recorded with the ***E***-vector parallel to the film surface (i.e., s-polarization, $\omega = 90°$). This measurement geometry and polarization angle provides maximum XMLD contrast for domains with their AFM spin axis oriented along in-plane $<110>_{pc}$ directions. A strong correlation is found between the AFM domain formation and the orientation of the line patterns with respect to the film in-plane crystalline axes. For the 2μm wide

lines (Fig. 3b), extended domains are observed near the edges, framing a central band with domains resembling those seen in blanket films. The domain contrast, and thus the direction of the AFM spin axis for these extended "edge domains", is determined by the crystalline orientation of the edge. For edges parallel to the $[110]_{pc}$ direction, the extended domains show dark contrast, whereas for edges parallel to the $[-110]_{pc}$ direction, the domain contrast is bright. When the linewidth is reduced (cf. Fig. 3(c) and (d)), the edge-induced domain ordering becomes more pronounced. The domain structure of 500nm wide lines appears to be governed by this *edge effect* across the full width of these nanowires. Moreover, we note that these extended domains are noticeably larger than the typical domains of blanket films, which is taken as evidence that the AFM spin axis has rotated as a result of the patterning.

Figure 4(a) and (b) compare the AFM domain structure of 100 nm wide zigzag line patterns with their edges parallel to in-plane $<110>_{pc}$ and $<100>_{pc}$ crystalline axes, respectively. In either case, the polarization angle ω was chosen so as to provide maximum contrast for domains with their spins oriented parallel to the nanowire edges. We observe a pronounced *edge effect* for nanowires aligned with both sets of in-plane low-index axes ($<110>_{pc}$ and $<100>_{pc}$). This finding shows that the two different types of AFM *easy axes* in these LFO/LSMO bilayers can be selectively stabilized in embedded nanowires by proper one alignment relative to the LFO crystalline axes, (i.e., along $<100>_{pc}$ or $<110>_{pc}$).

We note that the AFM domains of the LFO/LSMO nanowires displayed in Fig. 4(a), stabilized by edges aligned with the in-plane $<110>_{pc}$ axes, show a dark contrast when the ***E***-vector is perpendicular to the AFM spin axis and bright contrast when the two vectors are parallel. For AFM domains stabilized by edges along the in-plane $<100>_{pc}$ axes, however (cf. Fig. 4(b)), the contrast is reversed. For a polarization angle of $\omega = 40°$, the in-plane projection of the ***E***-vector is near parallel to the $[010]_{pc}$

direction and the ***E***-vector is near normal to the $[100]_{pc}$ direction. Nonetheless, AFM domains with their spin axis oriented along the $[010]_{pc}$ direction show dark contrast and those with spin axis along the $[100]_{pc}$ direction show bright contrast. Hence, we observe opposite contrast (dark/bright) for $<110>_{pc}$- and $<100>_{pc}$-oriented domains with the same relative orientation of the ***E***-vector and the AFM spin axis. This contrast reversal derives from a change of sign in the XMLD signal, which is consistent with previous experiments and multiplet calculations by Czekaj et al..[27] This finding is also consistent with our previous XMLD-PEEM data for nanostructures defined in LFO/Nb:STO[17] with the AFM spin axis oriented along in-plane $<100>_{pc}$ crystalline axes only.

We also investigated nanostructures defined with their edges oriented along the in-plane $<100>_{pc}$ and $<110>_{pc}$ directions for LFO[20u.c.]/LSMO[80u.c.] and LFO[50u.c.]/LSMO[50u.c.] bilayers, in experimental geometries sensitive to AFM domains with their spin axes in either of these directions. In these films with a thicker LFO epilayer, no distinct *edge effect* was observed.

In conclusion, we have investigated the AFM domains in LFO thin films grown as epitaxial bilayers with LSMO on Nb:STO substrate. Our measurements show a distinct difference between the AFM domain structure in these layers and that previously reported for LFO grown directly on Nb:STO. In both systems, we observe domains with their AFM moments oriented along in-plane $<100>_{pc}$ crystalline axes . However, the present films, grown on LSMO, with a lower than cubic symmetry, also display domains with their spin axis oriented along in-plane <110> directions. Relying on a recently discovered phenomenon of AFM domain ordering in LFO nanostructures,[17] we were able to stabilize domains with their magnetic moments oriented selectively along the in-plane $<100>_{pc}$ and $<110>_{pc}$ directions. We show how this mechanism may govern the AFM domain formation in LFO nanowires, sufficiently thin and with appropriate orientation relative to the film in-plane crystalline axes. This finding, that AFM order can be stabilized in crystalline directions different from those of the easy

axes in bulk LFO by proper choice of substrate and nanostructure geometry is set to inspire further work on domain engineering in interfacially coupled magnetic oxide thin films.

Acknowledgements. The authors thank Yasuhide Nakamura for help with the chemical etching of the Cr hard-mask, and prof. Yuri Suzuki (UC Berkeley) for assistance with SQUID magnetometer measurements. A portion of this research was conducted at the Center for Nanophase Materials Sciences, which is sponsored at Oak Ridge National Laboratory by the Office of Basic Energy Sciences, U.S. Department of Energy. The Advanced Light Source is supported by the Director, Office of Science, Office of Basic Energy Sciences, of the U.S. Department of Energy under Contract No. DE-AC02-05CH11231. Partial funding for these experiments was obtained from the Norwegian Research Council under Contract Nos. 176656 and 190086.

References.

* folven@ntnu.no

1 A. T. Zayak, X. Huang, J. B. Neaton, and K. M. Rabe, Phys. Rev. B **74**, 094104 (2006).

2 D. Fuchs, E. Arac, C. Pinta, S. Schuppler, R. Schneider, and H. v. Löhneysen, Phys. Rev. B **77**, 014434 (2008).

3 C. A. F. Vaz, J. Hoffman, C. H. Ahn, and R. Ramesh, Adv. Mater. **22**, 2900 (2010).

4 C. Aruta, G. Balestrino, A. Tebano, G. Ghiringhelli, and N. B. Brookes, Europhys. Lett. **80**, 37003 (2007).

5 S. Picozzi, C. Ma, Z. Yang, R. Bertacco, M. Cantoni, A. Cattoni, D. Petti, S. Brivio, and F. Ciccacci, Phys. Rev. B **75**, 094418 (2007).

6 J. H. Song, T. Susaki, and H. Y. Hwang, Adv. Mater. **20**, 2528 (2008).

7 H. S. Kim and H. M. Christen, J. Phys.: Condens. Matter **22**, 146007 (2010).

8 J. M. D. Coey, M. Viret, and S. von Molnar, Adv. Phys. **48**, 167 (1999).

9 Y.-H. Lee, J.-M. Wu, and C.-H. Lai, Appl. Phys. Lett. **88**, 042903 (2006).

10 H. Boschker, M. Mathews, E. P. Houwman, H. Nishikawa, A. Vailionis, G. Koster, G. Rijnders, and D. H. A. Blank, Phys. Rev. B **79**, 214425 (2009).

11 J. He, A. Borisevich, S. V. Kalinin, S. J. Pennycook, and S. T. Pantelides, Phys. Rev. Lett. **105**, 227203 (2010).

12 D. Ruzmetov, et al., Adv. Mater. **17**, 2869 (2005).

13 H. Hopster and H. P. Oepen eds., *Magnetic Microscopy of Nanostructures* (Springer-Verlag, Berlin Heidelberg, 2005).

14 M. Mathews, R. Jansen, G. Rijnders, J. C. Lodder, and D. H. A. Blank, Phys. Rev. B **80**, 064408 (2009).

15 E. J. Kim, J. L. R. Watts, B. Harteneck, A. Scholl, A. Young, A. Doran, and Y. Suzuki, J. Appl. Phys. **109**, 07D712 (2011).

16 H. V. Gomonay and V. M. Loktev, Phys. Rev. B **75**, 174439 (2007).

17 E. Folven, T. Tybell, A. Scholl, A. Young, S. T. Retterer, Y. Takamura, and J. K. Grepstad, Nano Lett. **10**, 4578 (2010).

18 A. M. Glazer, Acta Crystallogr B **B 28**, 3384 (1972).

19 P. M. Woodward, Acta Crystallogr B **53**, 32 (1997).

20 A. Vailionis, H. Boschker, W. Siemons, E. P. Houwman, D. H. A. Blank, G. Rijnders, and G. Koster, Phys. Rev. B **83**, 064101 (2011).

21 Y. Takamura, R. V. Chopdekar, A. Scholl, A. Doran, J. A. Liddle, B. Harteneck, and Y. Suzuki, Nano Lett. **6**, 1287 (2006).

22 A. Scholl, et al., Science **287**, 1014 (2000).

23 Principal component analysis is a multivariate statistical analysis technique suitable for identification of significant features in large data sets and for reducing random noise. See M. G. Burke, M. Watanabe, D. B. Williams, and J. M. Hyde, J. Mater. Sci. 41, 4512 (2006).

24 D. Alders, L. H. Tjeng, F. C. Voogt, T. Hibma, G. A. Sawatzky, C. T. Chen, J. Vogel, M. Sacchi, and S. Iacobucci, Phys. Rev. B **57**, 11623 (1998).

25 J. Stohr, A. Scholl, T. J. Regan, S. Anders, J. Luning, M. R. Scheinfein, H. A. Padmore, and R. L. White, Phys. Rev. Lett. **83**, 1862 (1999).

26 J. Luning, F. Nolting, A. Scholl, H. Ohldag, J. W. Seo, J. Fompeyrine, J. P. Locquet, and J. Stohr, Phys. Rev. B **67**, 214433 (2003).

27 S. Czekaj, F. Nolting, L. J. Heyderman, P. R. Willmott, and G. van der Laan, Phys. Rev. B **73**, 020401 (2006).

28 P. W. Anderson, Phys. Rev. **79**, 350 (1950).

29 J. W. Seo, E. E. Fullerton, F. Nolting, A. Scholl, J. Fompeyrine, and J. P. Locquet, J. Phys.: Condens. Matter **20**, 264014 (2008).

30 I. S. Lyubutin, T. V. Dmitrieva, and A. S. Stepin, J. Exp. Theor. Phys. **88**, 590 (1999).

31 Y. Takamura, unpublished.

FIG. 1. (color online) (a) XMLD-PEEM images showing the same 5 µm x 5µm blanket region for three polarization angles. A region showing uniform contrast for ω = 90° is outlined as a guide to the eye. (b) Recorded XMLD intensity vs. polarization angle, ω. The measurement geometry is illustrated in the inset. (c) Distribution of <110>- and <100>-oriented AFM domains as a function of LFO thickness. The inset shows the relative XMLD signal vs. LFO layer thickness.

FIG. 2. (color online) Linear q_x scans of the $(-204)_{pc}$ and $(204)_{pc}$ reflections in thin films and substrate for (a,b) LFO[100u.c.]/LSMO[50u.c.]/Nb:STO sample and (c,d) LFO[100u.c.]/Nb:STO sample. The peaks are all fitted using pseudo-Voigt curves (solid lines).

FIG. 3. (color online) (a) Schematic of the embedded nanostructures and the pattern layout. (b-d) XMLD-PEEM micrographs of the AFM domain structure of zigzag line patterns defined in LFO[10u.c.]/LSMO[90u.c.] bilayers with (b) 2µm,(c)1µm and (d) 500nm linewidths. The experimental geometry is illustrated in the inset in the lower left corner of each XMLD-PEEM image.

FIG. 4. (color online) XMLD-PEEM images of 100 nm wide zigzag nanostructures defined in an LFO[10u.c.]/ LSMO[90u.c.] bilayer; (a) with the nanostructure edges parallel to the in-plane <110> axes, and (b) with the edges parallel to the in-plane <100> axes, recorded with x-ray polarization angles (a) ω = 90° and (b) ω = 40°.

FIG.1.:

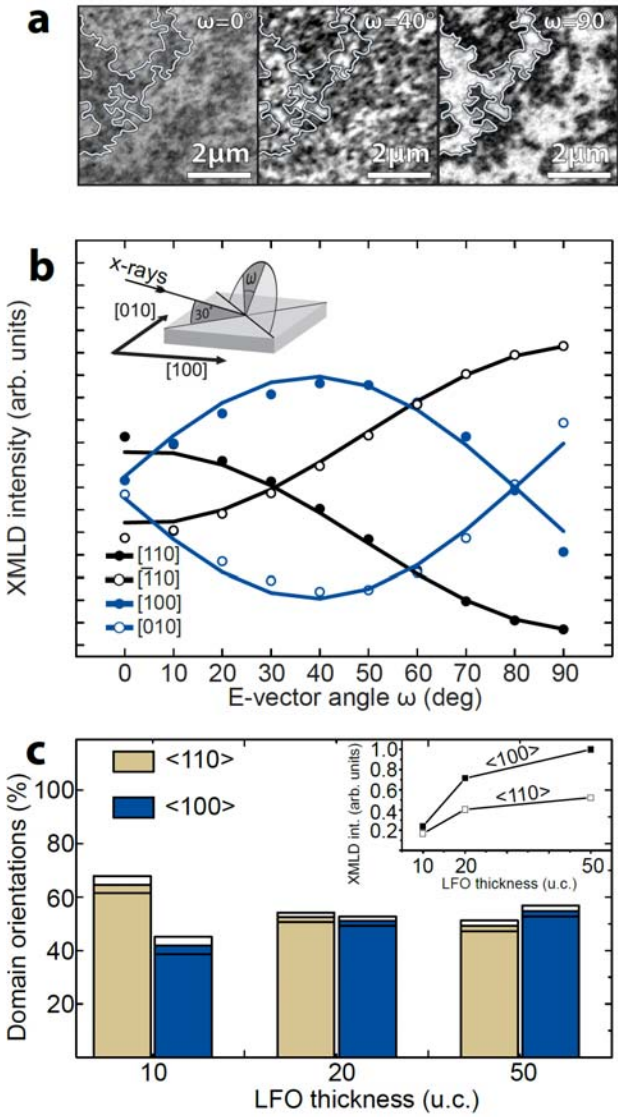
a
ω=0°
ω=40°
ω=90°
2μm
2μm
2μm
b
x-rays
[010]
[100]
30°
ω
XMLD intensity (arb. units)
[110]
[1̄10]
[100]
[010]
0 10 20 30 40 50 60 70 80 90
E-vector angle ω (deg)
c
<110>
<100>
Domain orientations (%)
100
80
60
40
20
10
20
50
LFO thickness (u.c.)
XMLD int. (arb. units)
1.0
0.8
0.6
0.4
0.2
<100>
<110>
10 20 50
LFO thickness (u.c.)

FIG.2.:

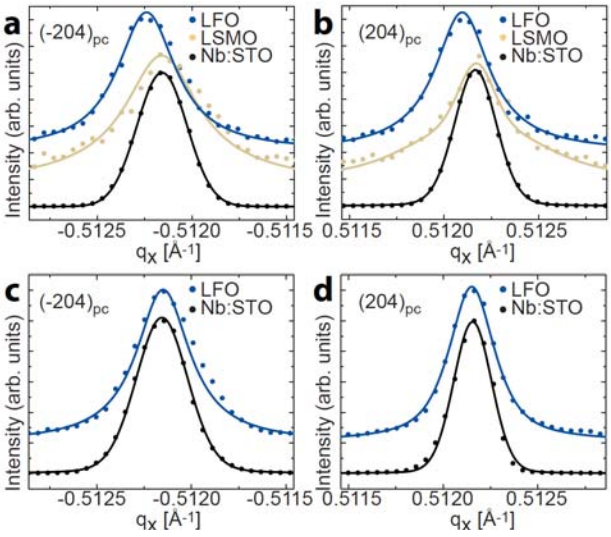
a
(-204)pc
LFO
LSMO
Nb:STO
Intensity (arb. units)
-0.5125
-0.5120
-0.5115
qx [Å-1]
b
(204)pc
LFO
LSMO
Nb:STO
Intensity (arb. units)
0.5115
0.5120
0.5125
qx [Å-1]
c
(-204)pc
LFO
Nb:STO
Intensity (arb. units)
-0.5125
-0.5120
-0.5115
qx [Å-1]
d
(204)pc
LFO
Nb:STO
Intensity (arb. units)
0.5115
0.5120
0.5125
qx [Å-1]

FIG.3.:

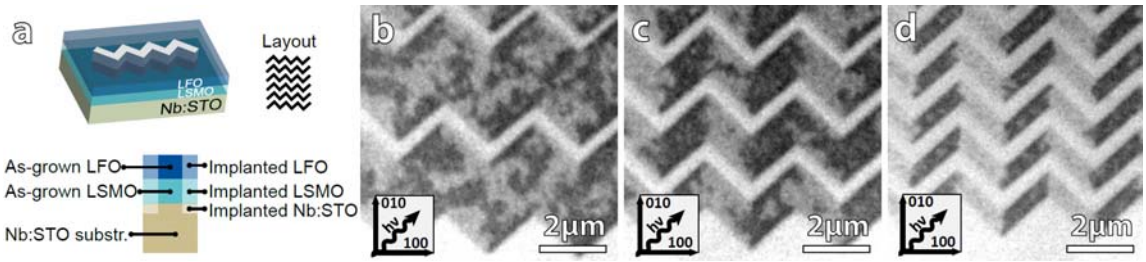
a
LFO
LSMO
Nb:STO
Layout
As-grown LFO
As-grown LSMO
Nb:STO substr.
Implanted LFO
Implanted LSMO
Implanted Nb:STO
b
c
d
010
100
2μm

FIG.4.: